Centrality dependence of longitudinal and transverse baryon distributions in ultrarelativistic nuclear collisions

J. Barrette,[3] R. Bellwied,[8] P. Braun-Munzinger,[7] W. E. Cleland,[5] T. M. Cormier,[8] G. David,[7] J. Dee,[7] G. E. Diebold,[9] O. Dietzsch,[6] J. V. Germani,[9] S. Gilbert,[3] S. V. Greene,[9] J. R. Hall,[4] T. K. Hemmick,[7] N. Herrmann,[2] B. Hong,[7] K. Jayananda,[5] D. Kraus,[5] B. S. Kumar,[9] R. Lacasse,[3] D. Lissauer,[1] W. J. Llope,[7] T. W. Ludlam,[1] S. McCorkle,[1] R. Majka,[9] S. K. Mark,[3] J. T. Mitchell,[9] M. Muthuswamy,[7] E. O'Brien,[1] C. Pruneau,[3] M. N. Rao,[7] F. Rotondo,[9] N. C. daSilva,[6] U. Sonnadara,[5] J. Stachel,[7] H. Takai,[1] E. M. Takagui,[5] T. G. Throwe,[1] C. Winter,[9] G. Wang,[3] D. Wolfe,[4] C. L. Woody,[1] N. Xu,[7] Y. Zhang,[7] Z. Zhang,[5] and C. Zou[7]
(E814 Collaboration)
[1]*Brookhaven National Laboratory, Upton, New York 11973*
[2]*Gesellschaft für Schwerionenforschung, Darmstadt, Germany*
[3]*McGill University, Montreal, Canada H3A 278*
[4]*University of New Mexico, Albuquerque, New Mexico 87131*
[5]*University of Pittsburgh, Pittsburgh, Pennsylvania 15260*
[6]*University of São Paulo, São Paulo, Brazil*
[7]*SUNY, Stony Brook, New York 11794*
[8]*Wayne State University, Detroit, Michigan 48202*
[9]*Yale University, New Haven, Connecticut 06511*
(Received 5 August 1994)

Inclusive double differential multiplicities $d^2N/dy\,dp_t$ and related quantities have been measured for protons and deuterons produced in 14.6A GeV/c Si + Al and Si + Pb collisions using the E814 forward spectrometer at the AGS at BNL. Collision "centrality" is determined by measuring N_c, the total charged particle multiplicity in the pseudorapidity range $0.85 < \eta < 3.8$. For both systems Si + Al and Si + Pb, an increase in the proton rapidity distribution dN/dy at midrapidity and a corresponding decrease at higher rapidities are observed with increasing N_c. For Si + Pb, Boltzmann slope parameters T_B increase significantly in the most central collisions. The measured distributions exhibit a centrality dependence even when $\sigma/\sigma_{\rm geo} \lesssim 10\%$, where full overlap between the Si and Pb nuclei occurs in a simple geometric picture. The proton rapidity distribution dN/dy is presented for the symmetric system Si + Al over the entire rapidity interval. The total number of protons, which is the integral of this quantity over rapidity, varies with N_c. Results are compared with various model calculations, mostly using the hadronic cascade codes ARC and RQMD. No significant nuclear transparency is observed, indicating that large baryon and energy densities are produced in these collisions.

PACS number(s): 25.75.+r

I. INTRODUCTION

Study of the distribution of baryons after ultrarelativistic heavy ion collisions can yield important information about the energy densities achieved. In particular, the distribution dN/dy of baryons in rapidity $y \equiv \frac{1}{2}\ln[(E+p_z)/(E-p_z)]$—where p_z is the longitudinal component of momentum, E is the energy, and the speed of light c is the unit of velocity—is directly related to the energy loss by the target and projectile nucleons during the collision. At very high energies, where the interval between the target and beam rapidities is large, even sizable rapidity shifts of the nucleons (e.g., $\Delta y \approx 2$, implying that the nucleons lose more than 90% of their energy during the collision) will leave the central rapidity region nearly empty. This implies small baryon density at central rapidity; target and projectile are "transparent" to each other [1].

At lower energies, however, the rapidity interval between target and projectile is small, so transparency will imply small rapidity shifts, and thus little energy loss and low energy density. To determine whether at AGS energies we are in the uninteresting regime of transparency or the interesting regime of stopping, we have measured proton and deuteron phase-space distributions. Initially, the target and projectile protons have rapidity distributions centered at $y_T = 0$ and $y_P = 3.44$, respectively, with widths of about 0.17 rapidity unit from Fermi motion, and the rapidity density $dN/dy = 0$ in between these two peaks. If the nuclei were highly transparent to each other, one might expect to see some broadening and small shift toward midrapidity of the initial distributions and a sparse population of the central rapidity region in the final state; the final proton distribution would exhibit peaks at or near target and beam rapidities. On the other hand, if the nuclei, colliding at zero impact parameter, are fully stopped, one would expect most of the nucleons at midrapidity, with the width of the distribution determined by thermal and possibly hydrodynamic motion, and no peaks in the beam and target regions.

Proton transverse momentum distributions $d^2N/dy\,dp_t$ offer a measure of the amount of equilibration or thermalization the system undergoes and reflect the actual temperature in a thermal model.

A first account of some of the following results has been given in Ref. [2]. Here we discuss in more detail the experimental procedure, centrality dependence and other systematics. In addition, deuteron data are presented, completing our measurement of baryon number density in phase space.

II. APPARATUS

The data presented here were obtained in March 1991 with the E814 apparatus (Fig. 1), most notably its forward spectrometer, at the Alternating Gradient Synchrotron (AGS) at Brookhaven National Laboratory (BNL). In what follows, we will refer to a right-handed coordinate system defined with origin at the intersection of beam and target, the z axis in the direction of the incident beam and y axis vertically upward. Consequently the x axis points to the left if the experiment is viewed from the vantage of the beam or upward in Fig. 1. For this portion of the 1991 run, we replaced the participant calorimeter (PCal) that usually stands downstream of the target and has a small opening with a lead collimator that accepts particles emitted into $-115 < \theta_x < 14$ mrad and $|\theta_y| < 21$ mrad, an acceptance much larger than that of the PCal opening ($\theta \lesssim 14$ mrad). We also removed the second spectrometer magnet (not shown) and shifted the first in the negative x direction. All this served to extend considerably the acceptance of the forward spectrometer in p_x and hence transverse momentum.

Upstream of the target are located two silicon microstrip beam vertex detectors (BVER's) with 50 μm pitch between strips that run in the y direction. These measure the incident beam trajectory in each event. The multiple-scattering dominated resolution is about 40 μrad in the incident beam angle and 80 μm in the x coordinate of the beam at the target. The "centrality" or violence of the collisions is determined by N_c, the total multiplicity of charged particles in the range $0.85 < \eta < 3.8$, as detected by a silicon pad detector (MULT) located downstream of the target [3], where $\eta \equiv -\ln\tan(\theta/2)$ is the pseudorapidity.

Charged particles produced in the forward direction either stop in the collimator or pass through its aperture to be momentum analyzed by the dipole spectrometer magnet and detected by two tracking chambers (DC2 and DC3), each of which has six drift planes with 300 μm resolution in the x direction. Each also has a segmented cathode plane with chevron-shaped pads providing millimeter resolution in the y coordinate. The size and corresponding resolution of the pads varies across each chamber according to the anticipated density of charged particle tracks.

After passing through the tracking chambers, charged particles are detected by a hodoscope of 10 cm wide plastic scintillation counters (FSCI's). One group of these scintillators sits 12 m from the target and has better than 200 ps time resolution; the second set sits 31 m from the target and has 350 ps resolution. The mass resolution due to the time resolution δt is $\delta m/m = (\delta t/z)\,\beta\gamma^2$. For the downstream counters, from which most of the present data are obtained, $\delta t/z = 0.3\%$. Since all particles accepted in the spectrometer are close to minimum ionizing or higher in momentum, the pulse height from the scintillators allows measurement of the magnitude of the charge of the particles striking them. The empty space between DC2 and DC3, as well as that between DC3 and the downstream scintillators, is occupied by bags of helium to minimize the effects of reinteraction and multiple scattering.

III. ANALYSIS

A. Momentum measurement

The hits in the various detectors downstream of the magnet are reconstructed into tracks by an E814 pattern recognition program called "Quanah," based on the tree-climbing algorithm of Cassel and Kowalski [4]. Quanah is also discussed in some detail in Ref. [5].

Hits in the drift section of a chamber are reconstructed into partial tracks called *elements*, comprising hits in at least three of the six wire planes in a chamber. Each element is projected to the pad plane of the chamber to look for pad hits called *clusters*. A cluster is formed under a given wire by looking for the pad with the most

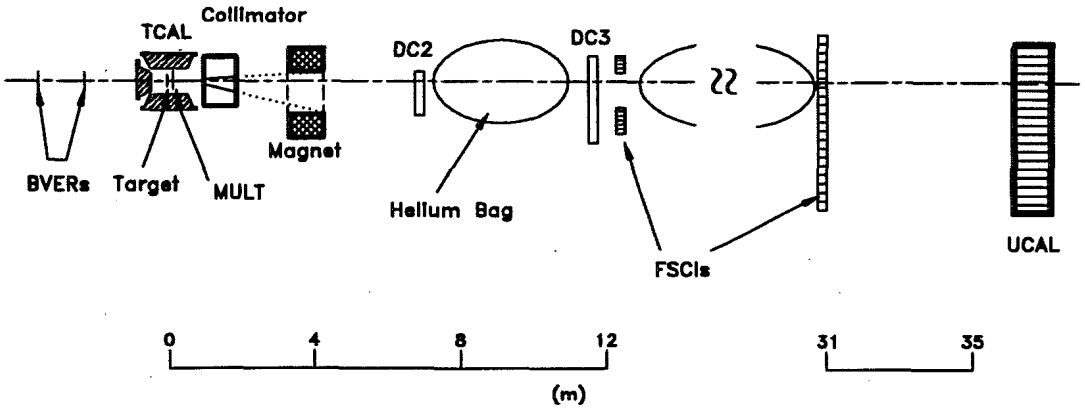

FIG. 1. The E814 apparatus.

charge on it and computing the charge-weighted centroid $y_{\rm cent}$ of the y positions of that pad and its neighbors. This centroid $y_{\rm cent}$ still needs to be corrected for some nonlinearity in the charge sharing between pads; $y_{\rm cent}$ is mapped to an actual position via a calculation involving the induced charge on the pad plane from a point charge on the associated wire. The induced charge was used to compute $y_{\rm cent}$ as a function of the actual y position. This map then allows determination of the actual y position of the charge on the wire from the measurement of $y_{\rm cent}$. The result of this calculation for one region of DC2 is shown in Fig. 2.

If a cluster is found on the pad plane matching the projected position of an element, the associated vertical position information is used. If no cluster is found, an inefficiency is avoided by using the element alone with no vertical position information. This is necessary because in the region where the beam traverses the chamber, the heavy ion saturates the ADC for the pads it crosses. These pads cannot provide useful information for minimum-ionizing particles that cross them close in time to the beam.

Hits from each chamber are combined with hits in the scintillators to form *segments*. The algorithm requires that the segments be straight within the detector resolutions, and based on the apparatus geometry, we place a loose cut on the angles they make with the beam axis. Position information in both dimensions is available from the scintillators, though with limited resolution. The horizontal position is specified by the hodoscope granularity to within ± 5 cm, and the vertical position is obtained either from the time or amplitude signals from the phototubes at each end of the scintillator slats. The resolution in this coordinate is 3–4 cm, comparable to the resolution in the horizontal coordinate.

Segments that point back into the magnet aperture are assigned vector momenta, becoming *candidates*. Since the apparatus in this configuration has no tracking between the target and the magnet, determination of the momenta requires assuming that the candidates originated where the beam struck the target. Each component of the magnetic field has been measured as a function of position inside and near the magnet. We have determined that the effect of the fringe field can be accurately accounted for by using an effective length somewhat greater than the length of the magnet itself. This allows us to model the apparatus as a region of uniform magnetic field with only a y component surrounded by a region of zero field.

With these assumptions, we can make the following statements (see Fig. 3):

$$R(\sin\theta' - \sin\theta) = -\ell, \tag{1}$$

$$x = z\tan\theta, \tag{2}$$

$$x' - x = R(\cos\theta' - \cos\theta), \tag{3}$$

where R is the radius of the circular projection onto the bend plane of the helical trajectory of the track through the region of magnetic field, with the convention that $R > 0$ if a particle is deflected in the $-x$ direction, as shown in Fig. 3. Note that x and x' are measured relative to the vertex x position, as determined by the vertex detector. The angle the particle's trajectory makes in the bend plane with the z axis before the magnet is θ, and that after the magnet is θ'. The effective length of the magnetic field region is denoted by ℓ. The radius of curvature R is related to the magnetic rigidity p_{zx}/Z by

$$R = \frac{p_{zx}}{ZeB}, \tag{4}$$

where $p_{zx} \equiv \sqrt{p_x^2 + p_z^2}$ is the momentum component in the bend plane, e is the proton charge, Z is the particle's charge number, and B is the magnitude of the magnetic field. The exact value of B is verified by comparing the known beam momentum and the measured momentum of beam-rapidity protons.

Combining Eqs. (1) and (3) we eliminate R:

$$\frac{\sin\theta - \sin\theta'}{\ell} = \frac{\cos\theta' - \cos\theta}{x' - x}. \tag{5}$$

Equation (2), along with some trigonometry, allows us to eliminate θ, so we have

$$\frac{x - \sin\theta'\sqrt{x^2 + z^2}}{\ell} = \frac{\cos\theta'\sqrt{x^2 + z^2} - z}{x' - x}. \tag{6}$$

Moving the radicals to one side and squaring gives a fourth order polynomial in x, the algebraic solution of which is straightforward, if tedious. The closed form of

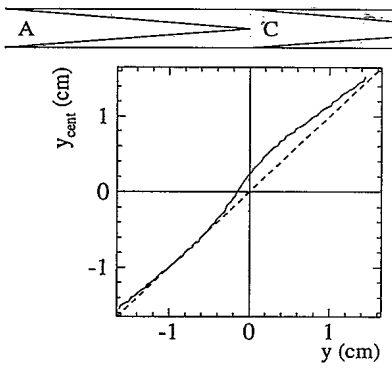

FIG. 2. Position calculated from the charge centroid of three pads vs actual position in the high-density region of DC2. The actual geometry of three such pads, labeled A, B, and C, is shown above the plot on the same scale.

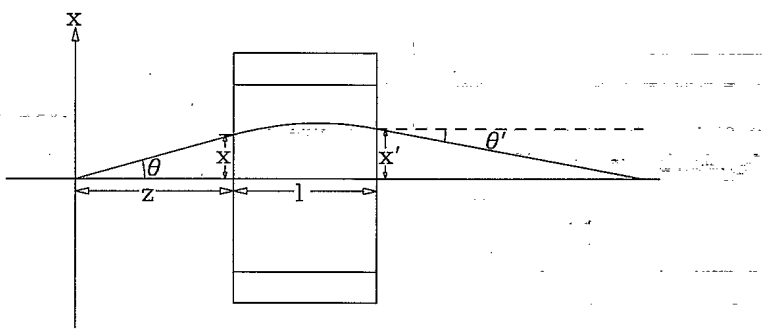

FIG. 3. Bend-plane geometry of a track passing through a region of uniform magnetic field.

the solution is too cumbersome to be useful, but an algorithm exists for computing the roots of an arbitrary quartic equation [6]. The position x at the entrance to the magnet determines θ and R, and hence p_{zx}/Z, via Eqs. (1)–(4). In practice, an iterative numerical procedure is used to find these quantities.

In an ideal dipole magnet, the component p_y of momentum parallel to the magnetic field is conserved, as is p_{zx}, the magnitude of the component normal to the field. Hence, the out-of-plane angle $\phi \equiv \arctan(p_y/p_{zx})$ is conserved, so the vertical component of momentum may be reconstructed by using the vertical position information from the detectors to measure ϕ and multiplying p_{zx}, obtained from the previous procedure, by $\tan\phi$.

Candidates may occasionally share hits in the various detectors. A final algorithm selects the largest subset of the candidates that share no hits. These candidates are finally the reconstructed *tracks* produced by Quanah.

Using the charge magnitude measured via the energy loss in the scintillators, we determine the momentum of each particle. For the value of the magnetic field used, the field integral $\int B \cdot dl$ is 0.273 T·m, and the momentum resolution corresponding to the 300 μm position resolution of the chambers is $\delta p/p \approx (0.1\%/\mathrm{GeV})\, pc/|Z|$. The momentum resolution over our momentum range is dominated by multiple scattering in the apparatus, mostly in the 7 m of air between the target and DC2; this contribution is $\delta p/p \approx 3.6\%/\beta$, where β is the particle's velocity relative to the speed of light. The transverse momentum resolution is dominated by multiple scattering and has the form $\delta p_t/p_t = \beta^{-1}\sqrt{\alpha_1^2 p_t^{-2} + \alpha_2^2}$, where $\alpha_2 = 3.6\%$, independent of target. For the thickest Pb target (2% nuclear interaction length), α_1 takes its largest value of 6.2 MeV. At $p_t = 0$, the resolution is $\delta p_t = \alpha_1/\tanh y$. At $y = 1$ this is $\delta p_t = 8.1$ MeV.

B. Particle identification

Reconstruction of the tracks also allows measurement of the lengths of the total flight paths of the particles, which together with the time of flight determined by the scintillators, yields the velocity β of each particle. The time of flight indicated by each photomultiplier tube is corrected for "slewing," the dependence on pulse height of the time indicated by the TDC. After the slewing correction is applied, we determine the mean time of the top and bottom tubes. To find the time offset t_0 for every counter, we employ an iterative procedure, using the measurement of velocity and momentum, and hence the mass, associated with each track. Having identified protons and pions, we use their known masses and well-determined momenta to predict their times of flight, hence obtaining t_0.

The measurement of β, together with the momentum measurement, determines the mass of each particle (Fig. 4). We identify particles with mass resolution that is good at low momenta and deteriorates gradually with increasing momentum, though still allowing separation of protons from pions up to a momentum of about 7 GeV/c. Protons can only be separated from kaons below 2 or 3 GeV/c, but the kaon rate is very low, and most of the scintillators lie 31 m from the target after which distance most kaons will have decayed, so there is essentially no kaon background in the proton mass peak. Protons and deuterons are identified by a momentum-dependent mass cut for $\beta < 0.988$ and $p < 10$ GeV/c. Outside of this region, protons are identified by a cut in the $1/\beta$-Z/p plane as indicated by the trapezoid in Fig. 4.

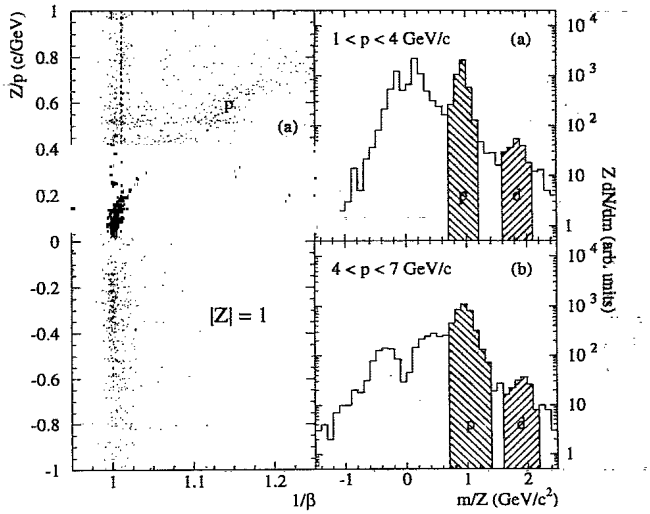

FIG. 4. Particle identification by measurement of velocity β and rigidity p/Z for $|Z| = 1$. Solid lines in the left-hand panel mark the boundaries between the momentum bins, labeled a and b, on the right-hand side, for $Z = +1$. Above and to the right of the dashed lines in the left panel, particles are identified by mass cuts illustrated by the hatched regions in the two right panels. Tracks that fall in the region containing $\beta = 1$ and $p = 10$ GeV/c indicated by the trapezoid in the left panel are also assumed to be protons (see text).

C. Acceptance

Protons are accepted in the phase space region indicated by the contour lines in the left panel of Fig. 5 determined by the distribution of protons measured in the spectrometer. Fluctuations in the contour lines are due to limited statistics. The right-hand contour of the acceptance is a line at $p = 22$ GeV/c, above which beam rapidity deuterons become a significant background. Between 9 and 22 GeV/c, we cannot distinguish protons from deuterons, but as discussed in Sec. IV C below, the deuteron-proton ratio is low enough that the background introduced by assuming all tracks in the trapezoidal region of Fig. 4 are protons is on the percent level. The pion-proton ratio at these momenta is even lower. The left-hand contour is determined by the geometry of the apparatus and the magnitude of the magnetic field. Note that for $y \geq 1.5$ the acceptance includes $p_t = 0$, and we accept low p_t protons even below $y = 1$, allowing precise measurement of the low p_t part of the spectra to very low rapidities. For $y \geq 2.4$ we accept most, if not all, protons, regardless of their transverse momenta, and we have good sensitivity to the shapes of the transverse momentum spectra; conversely, below $y = 2.4$ we lose sensitivity to the shapes and accept a decreasing fraction

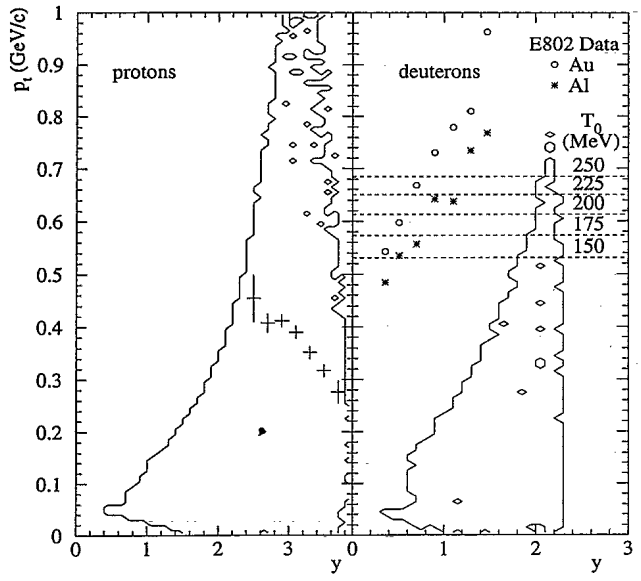

FIG. 5. Phase space acceptance of the E814 forward spectrometer for protons and deuterons. Solid crosses in the proton plot indicate the most likely transverse momentum as a function of y. For deuterons, the location $\sqrt{m_d T_0}$ of a hypothetical peak for various values of a slope parameter T_0 is given by dashed lines. The peak locations observed by E802 in central collisions are plotted also [7].

of the protons with decreasing rapidity.

Deuterons are accepted in the phase space region indicated in the right panel of Fig. 5. The right-hand contour of the acceptance is a line at $p = 9$ GeV/c. Above this momentum it is impossible to separate deuterons from protons via time of flight measurement. The left-hand contour is again determined by geometry and the magnetic field. Also indicated in Fig. 5 is the most probable transverse momentum for each rapidity bin. For the protons this information is obtained from our measured spectra (see Sec. IV A below). For deuterons we use the values of T_0 [see Eq. (9) below] measured by E802 [7]; note that because in each case T_0 is much smaller than the deuteron mass, to leading order in T_0/m_d the most probable transverse momentum is given by $\sqrt{m_d T_0}$. The dashed lines are the most probable transverse momenta for deuteron inverse slope parameters from 150 to 250 MeV.

For each rapidity y and transverse momentum p_t we accept a different fraction of the protons and deuterons produced. For example, at and near $p_t = 0$, we accept all protons above rapidity 1.5, since the spectrometer lies on the beam axis; for this case, the geometric efficiency $\epsilon_{\rm geo}$ is unity. For larger p_t, $\epsilon_{\rm geo}$ decreases and eventually only particles generated with azimuthal angle ϕ near π ($p_x = -p_t$) will enter the spectrometer. In general, neglecting subtle effects, $\epsilon_{\rm geo}$ is equal to the fraction of 2π accepted in azimuth for a given y and p_t. To calculate the geometric efficiency, we use the GEANT detector simulation package [8], which allows proper implementation of the strength of the magnetic field and the intersection of various detector systems with the collimator opening. This calculation includes effects of beam divergence, multiple scattering, etc.

In the acceptance calculation, incident beam trajectories are determined randomly using the distributions measured by the BVER's. Both in the data and in the simulation, angles and hence y and p_t are measured relative to the measured or simulated horizontal beam angle on an event-by-event basis, rather than with respect to the fixed laboratory coordinate frame.

Also, both in the data and in the simulation, a fiducial cut is made inside the collimator acceptance, requiring $\theta_x < 10$ mrad and $|\theta_y| < 16$ mrad, since at the physical boundaries of the collimator opening, $\epsilon_{\rm geo}$ falls to 0 in a way dependent on the *exact* location of the collimator. Although these angles form the boundaries of our acceptance in p_y and positive p_x, they lie well within the acceptance in p_t, since θ_x may go out to -115 mrad. Hence, without this fiducial cut, any uncertainty in the collimator position would translate to large variations in the correction factor $1/\epsilon_{\rm geo}$, which could result in artificial structures in the p_t spectra.

An example of the geometric efficiency $\epsilon_{\rm geo}$ thus obtained is shown in Fig. 6 for $3.2 \leq y < 3.4$. The dip near $p_t = 50$ MeV/c is caused by excluding the scintillator slat crossed by the heavy ion beam. The raw data obtained from the spectrometer are divided by $\epsilon_{\rm geo}$ to produce final transverse momentum spectra.

D. Track reconstruction efficiency

In addition to the momentum-dependent geometric efficiency correction, a global (momentum-independent) correction has to be made for the efficiency of the tracking hardware and software. The hardware efficiency of the tracking chambers themselves is essentially 100%. In each chamber the pattern recognition code, Quanah, only requires three of the six wire planes to register the pres-

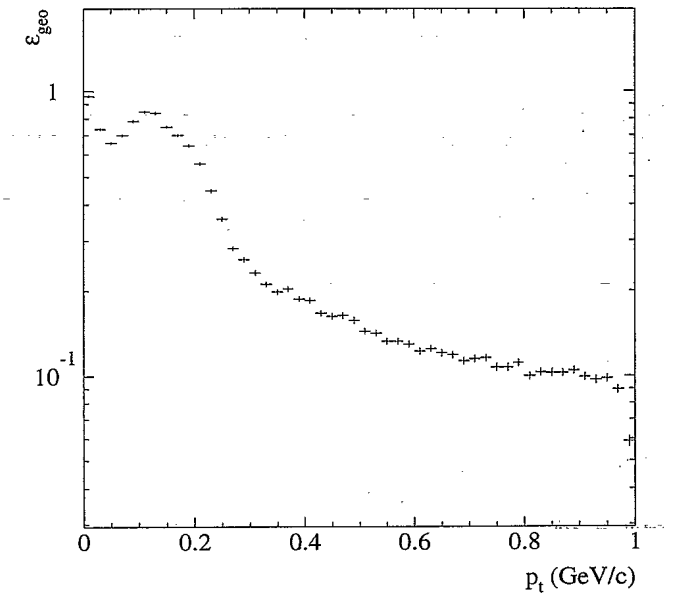

FIG. 6. Geometric efficiency for protons in the rapidity range $3.2 < y < 3.4$. Errors are due to the statistics of the Monte Carlo simulation.

ence of the track. The individual wire efficiency has been measured to be 90%. Since the number of wires firing is observed to obey a binomial distribution, the overall inefficiency of each chamber requiring three or more wires is about 10^{-3}. The pad planes are not required by Quanah for track reconstruction. If they are present, they are used, but the average track multiplicities in the spectrometer are low enough (about 5 for Si + Al, 1.5 for Si + Pb in typical central collisions) that the information from the drift sections is usually sufficient to reconstruct a track and point unambiguously to a scintillator for time of flight information. In addition, the scintillators downstream give information on the vertical coordinate though with considerably poorer resolution than the pad planes. The pad plane efficiency is around 95%, with the exception of the beam region (see above), so for most tracks the pad information is available. Even when pad information is not available, vertical position information is obtained from the scintillators, so vertical information is always present for the tracks considered in this analysis. Timing information will not be present for tracks that strike the same scintillator slat as the beam particle. The geometric inefficiency introduced by ignoring the scintillator beam region is taken into account in the computation described in Sec. III C above. Because the occupancy is low (around 10% in the case of Si + Al; 3% for Si + Pb) we can identify tracks with $|Z| = 1$ by a cut below three times and above half the pulse height of minimum ionizing particles. After this cut, the scintillator efficiency is about 90%. Because of the large distances between the various detectors, the overall efficiency of the reconstruction procedure is found to be 72% ±3% (stat) from visual inspection of about 250 events. We estimate an overall systematic uncertainty of about 10% on the normalization of the differential multiplicities presented below.

IV. RESULTS

A. Proton slope parameters

Figure 7 shows representative proton transverse mass spectra in selected rapidity bins for the Al and Pb targets. A set of transverse mass spectra for protons using the Pb target has already been presented in a previous publication [2]. Here we study mainly the systematic dependence of the slope parameters on centrality.

A purely thermal (Boltzmann) model predicts that the number d^3N of particles of a given species produced into an element of phase space d^3p satisfies

$$\frac{d^3N}{d^3p} \propto \exp\left(-\frac{E-\mu}{T}\right), \tag{7}$$

where T is the temperature of the source, E is the center-of-momentum energy associated with d^3p, and μ is the chemical potential. Expressed in terms of the invariant multiplicity, rapidity, and transverse mass $m_t \equiv \sqrt{m^2 + p_t^2}$, one finds

$$\frac{1}{p_t}\frac{d^2N}{dp_t\,dy} = \frac{1}{m_t}\frac{d^2N}{dm_t\,dy} = A_B(y)\frac{m_t}{m}\exp\left(-\frac{m_t-m}{T_B(y)}\right), \tag{8}$$

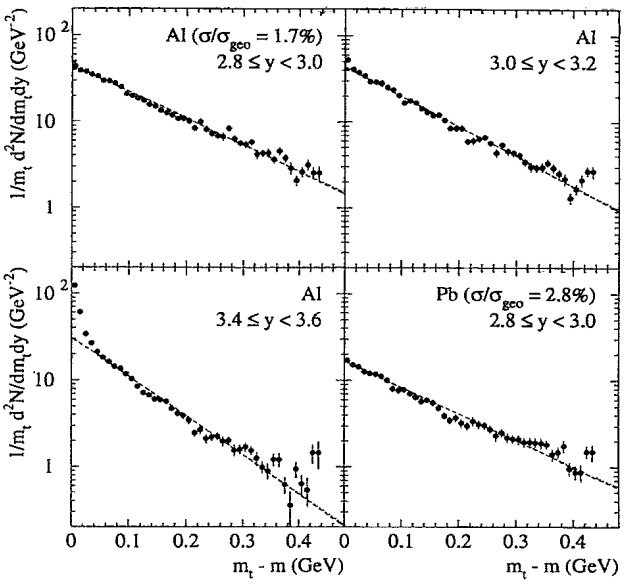

FIG. 7. Proton invariant yields vs transverse mass for 14.6A GeV/c Si + Al, Pb → $p + X$ at different rapidities. In each panel are plotted two fits: the dashed line is a Boltzmann curve, and the dotted line is an exponential. The two curves are virtually indistinguishable. Errors are statistical.

where $A_B(y) \propto m\cosh(y - y_{\text{c.m.}})\exp[\mu/T - m/T_B(y)]$ is the $p_t = 0$ intercept of the function at rapidity y, $y_{\text{c.m.}}$ is the center-of-momentum rapidity of the "fireball," and $T_B(y) = T/\cosh(y - y_{\text{c.m.}})$. This rapidity dependence of A_B and T_B only holds if the "fireball" emits isotropically. If the emission is not isotropic, the shape of the rapidity distribution and of $T_B(y)$ may vary, but if the system thermalizes, one still expects to see the general behavior indicated by Eq. (8).

Another convenient parametrization is

$$\frac{1}{p_t}\frac{d^2N}{dp_t\,dy} = \frac{1}{m_t}\frac{d^2N}{dm_t\,dy} = A_0(y)\exp\left(-\frac{m_t-m}{T_0(y)}\right), \tag{9}$$

which does not have a direct physical interpretation, but is often used to parametrize charged particle spectra in high-energy collisions. We will consider both parametrizations later on. The parameters A_0, A_B, T_0, and T_B are extracted in each rapidity bin by fitting the measured spectra.

As indicated in shown in Fig. 7 and previously discussed in Ref. [2], the Boltzmann spectra fit the data well, but m_t only varies by about 40% over the entire range covered, so there is no visible difference in our acceptance between a Boltzmann spectrum and one in which the invariant multiplicity or cross section is exponential in m_t, as in Eq. (9). Cole [9] has reached a similar conclusion for data from E802 for central Si + Au collisions. We choose the Boltzmann parametrization because there the slope has a direct physical interpretation as a temperature and can be compared with other measures of the temperature.

Near beam rapidity ($y_B = 3.44$) and $p_t = 0$, a steep component of the transverse momentum spectrum emerges (see Fig. 7), which we identify with "punch-

through" protons. These protons from the projectile traverse the target nucleus interacting at most elastically even in these central collisions. This component has been discussed in detail previously [5,10] and will not be further addressed here. In rapidity bins where this component is present, it has been excluded from the slope fits, but it is of course included when we later compute dN/dy by integrating over m_t.

Figures 8 and 9 show proton slope parameters T_B and T_0 vs rapidity y for several different centralities in the systems Si + Al and Si + Pb, respectively. The open symbols for the nearly symmetric system in Fig. 8 are reflections of the solid symbols about $y = 1.7$. In each figure, T_B is plotted in the top panel along with two extrapolations, labeled A and B, used later to compute dN/dy. In the bottom panel of each figure, T_0 from our measurement is plotted along with data from E802 [11] and extrapolations A′ and B′ of T_0 equivalent to the extrapolations A and B of T_B indicated in the top panel.

Now we wish to determine the degree to which T_B reflects the actual temperature of the system. Comparison of T_B with pion, kaon, lambda, and deuteron slopes [7,12,13] shows no dependence on beam momentum if rapidity is normalized to the beam rapidity and the same centrality is selected. The slope parameter T_B does increase systematically with particle mass, however, suggesting transverse expansion of the system with uniform

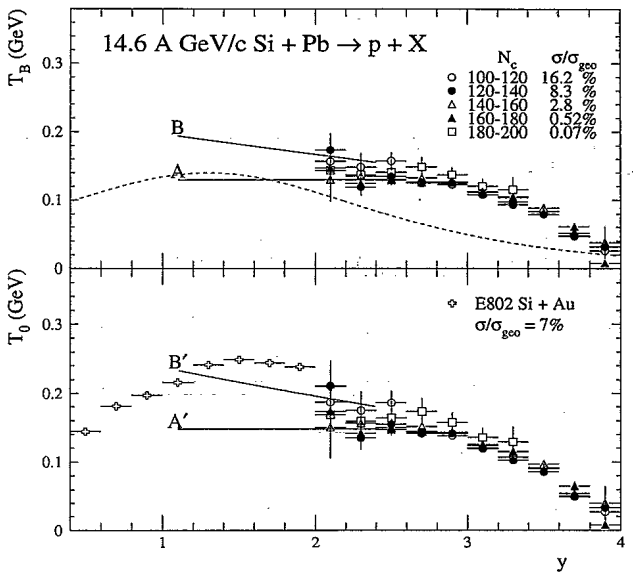

FIG. 9. Proton transverse mass inverse slope parameters as a function of rapidity for different centralities. The top panel shows the two extrapolations, labeled A and B, used to compute dN/dy. The bottom panel shows T_0 as measured by E802 [11] for the top 7% of the geometric cross section and two extrapolations, labeled A′ and B′ equivalent to A and B in the top panel. The dashed curve is the prediction of an isotropically emitting thermal model with 140 MeV temperature and center-of-momentum rapidity $y_{\text{c.m.}} = 1.3$.

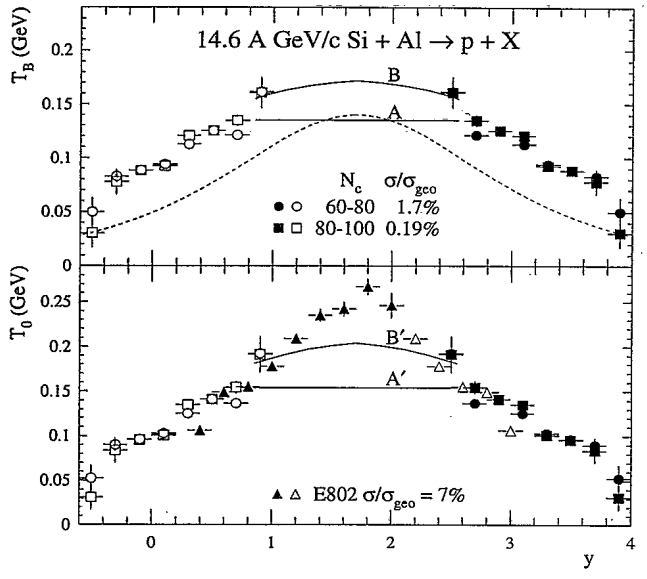

FIG. 8. Proton transverse mass inverse slope parameters as a function of rapidity for two different centralities. In each case, the data from $y > 2.4$ (solid symbols) are reflected about $y = 1.7$ and plotted for $y < 1.0$ (open symbols). The top panel also shows the two extrapolations, labeled A and B, used to obtain dN/dy. The bell-shaped dashed curve in the top panel indicates the prediction for an isotropically emitting thermal model with 140 MeV temperature. The results from E802 [11] are shown for the top 7% of the geometric cross section, again reflected about midrapidity. Also shown in the bottom panel are extrapolations A′ and B′ of T_0 equivalent to the extrapolations A and B of T_B in the top panel.

velocity. Since T_B is a measure of a particle's average transverse momentum, one expects a contribution from thermal motion in the form of a temperature and an additional contribution proportional to $m\gamma\beta_t$, where β_t is the mean transverse expansion velocity. If β_t is the same for all particle species, heavier particles will have larger mean transverse momenta, and larger values of T_B. An independent measure of the temperature is obtained from the population of nucleon resonances [14] and our data on pion spectra give a value of $T = 140 \pm 20$ MeV [13,15]. Using this temperature, simultaneous consideration of deuteron, proton, kaon, and pion transverse slopes has yielded an average transverse expansion velocity of 0.24–0.30 [16,17]. Costales performed a similar investigation, but without this additional constraint on the temperature, he obtained somewhat different numerical results [18].

If the system were emitting particles isotropically, one would expect to see slopes similar to what is indicated by the bell-shaped curves in the top panels of Figs. 8 and 9, i.e., $T_B = T\,\text{sech}(y - y_{\text{c.m.}})$, where $T \approx 140$ MeV is the system's temperature. The proton slope parameters lie well above these curves in each case, indicating a significant additional effect, such as the transverse flow discussed above. Longitudinal expansion, if present, will broaden the rapidity dependence of T_B, also raising the measured values at forward and backward rapidities. Note that in the absence of any other information, an isotropic model fit to the proton slopes alone would yield $T \gtrsim 225$ MeV for Si + Al and even higher values for Si

+ Pb. Such a high temperature is inconsistent with data on nucleon resonance populations [15] and slopes of pion transverse momentum spectra [11]. Furthermore, even assuming these high temperatures, an isotropic thermal model does not reproduce in detail the rapidity dependence shown in Figs. 8 and 9 (see also the discussion in Ref. [2]).

In Fig. 9 we see for $y > 2.6$ an increase in T_B in the most central collisions in each rapidity bin. To display more clearly the centrality dependence, we present in Fig. 10 T_B vs N_c for Si + Pb in several different rapidity bins. In each case we observe an increase in T_B with increasing centrality. This is demonstrated in the insert in Fig. 10, where we have plotted $\Delta T_B \equiv T_B|_{N_c=190} - T_B|_{N_c=110}$ vs rapidity. In each of the four bins, ΔT_B exceeds zero by at least one standard deviation. We know of no systematic error that could explain this effect. From a simple geometric model, one expects full overlap between the Si and Pb nuclei when $\sigma/\sigma_{\text{geo}} = 10\%$, or when $N_c \approx 120$, but the increase in T_B occurs well above that value. This effect may indicate the onset of a phase transition as predicted by van Hove [19] and borne out by later hydrodynamic calculations [20].

B. Proton rapidity distributions

As indicated in Fig. 5, the spectrometer's acceptance in p_t decreases rapidly below $y \approx 2.4$. Forward of this rapidity, most protons are accepted, regardless of their transverse momenta, and we have good sensitivity to T_B. Therefore, integrating the double differential multiplicity to the acceptance limit yields most of the rapidity distribution dN/dy, and we extend the integral to arbitrarily large p_t analytically using the parametrization in Eq. (8). Below $y \approx 2.4$, however, the integral to the acceptance limit forms a diminishing fraction of dN/dy and we cannot precisely determine the slope of the p_t spectrum; but we do measure the magnitude of the spectrum, in particular the intercept at $p_t = 0$. We can therefore deduce dN/dy in this region if we assume values for T_B by extrapolating the data from the region where we do measure them to the lower rapidities. The curves labeled A and B in the upper panel of each of Figs. 8 and 9 indicate two different extrapolations considered for each target. Using extrapolation A in each case forms essentially a lower bound on dN/dy since all available data show a systematic increase of slopes toward midrapidity [12], and dN/dy is an increasing function of T_B. We consider extrapolation B a more realistic estimate, but it places by no means an upper limit on dN/dy.

The squares and circles in Fig. 11 are the resulting rapidity distributions for Si + Al for two different centrality bins using for $y < 2.4$ extrapolation B. The results of using extrapolation A are indicated for each centrality by a line for $1.1 < y < 2.3$. The variation in dN/dy between the two different extrapolations gives us an estimate of about 20% for the systematic error on our measurement at midrapidity.

Although the parametrization given in Eq. (8) depends exponentially on T_B, dN/dy varies only slowly with the slope parameter. Most of the protons are produced at low values of p_t and our measurement fixes the $p_t = 0$

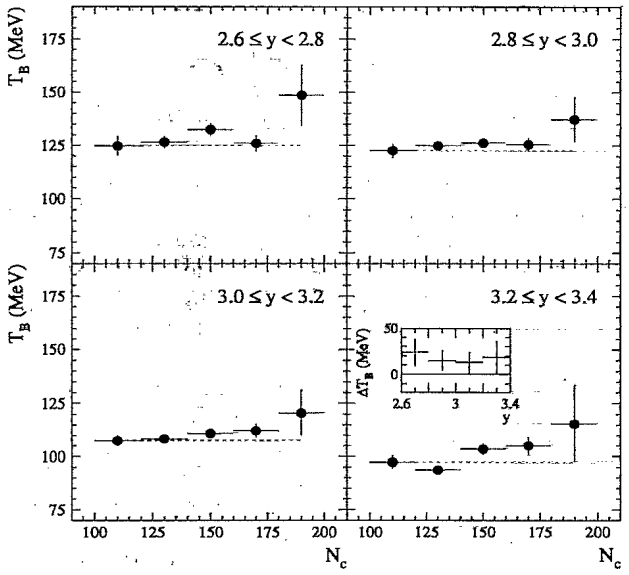

FIG. 10. Proton transverse mass inverse slope parameters T_B as a function of charged-particle multiplicity for Si + Pb in different rapidity bins. A horizontal line through the first data point is shown to illustrate the slope in the data. The insert in the last panel shows $\Delta T_B \equiv T_B|_{N_c=190} - T_B|_{N_c=110}$ with statistical error as a function of rapidity.

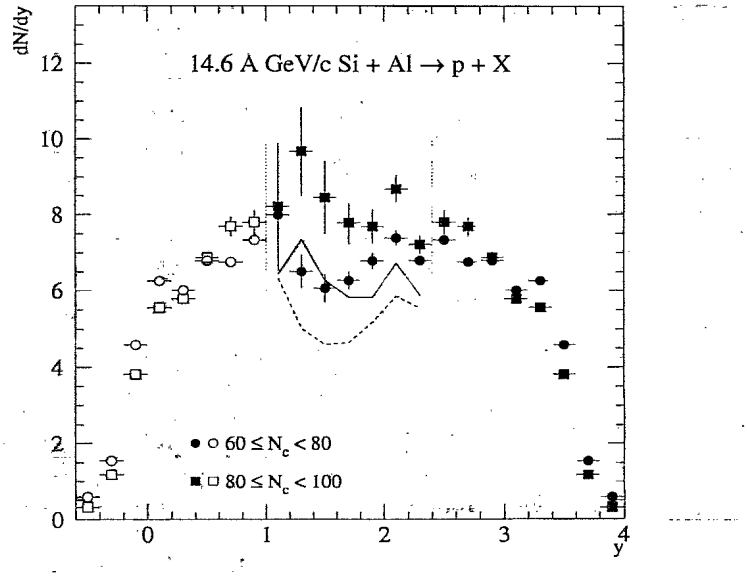

FIG. 11. Proton rapidity distributions for Si + Al, two different centralities. The points plotted for $1 < y < 2.4$ are the results of using extrapolation B of T_B (see Fig. 8). The solid line indicates the results of extrapolation A for the more central data. The dashed line is the same for the less central data. The vertical dotted lines at $y = 1.0$ and 2.4 delimit the region where we use extrapolated values of T_B to compute dN/dy.

intercept, A_B. Varying the slope makes the biggest difference at large p_t, where the yield is very small. More precisely, using the notation of Eq. (8):

$$\frac{dN}{dy} = \int_m^\infty \frac{d^2N}{dm_t\,dy} dm_t = A_B\, m T_B \left(1 + 2\frac{T_B}{m} + 2\frac{T_B^2}{m^2}\right). \tag{10}$$

Since T_B is considerably less than the proton mass and A_B is fixed by our measurement, dN/dy depends essentially linearly on T_B.

For the most central collisions, corresponding to $80 \leq N_c < 100$ or $\sigma/\sigma_{\rm geo} = 0.19\%$, the general shape of the rapidity distribution in the bottom panel of Fig. 12 is fairly flat over three units of rapidity, with no peak near beam rapidity, indicating no significant nuclear transparency even in this symmetric system. For a thermal system isotropically emitting protons, one expects from Eq. (10):

$$\frac{dN}{dy} \propto e^{-\alpha}\left(1 + 2\alpha^{-1} + 2\alpha^{-2}\right), \tag{11}$$

where $\alpha = (m/T)\cosh(y - y_{\rm c.m.})$. When $m = 938$ MeV/c^2, the proton mass, and $T = 140$ MeV, this distribution is well approximated by a Gaussian with $\sigma = 0.38$, a distribution much narrower than the data. The mean proton energy loss in the collision center-of-momentum frame computed from the upper half of the rapidity distribution in Fig. 12 is 0.91 GeV, 52% of the initial proton kinetic energy in this frame. The mean rapidity shift of projectile protons $\langle \Delta y \rangle$ is 0.85. This could be an indication of incomplete stopping: 61% compared to the value of $\langle \Delta y \rangle \approx 1.4$ computed from the isotropic distribution in Eq. (11) for $T = 140$ MeV.

Alternately, the larger width of the proton rapidity distribution may also indicate longitudinal expansion of the system after stopping. In the collision center-of-momentum frame, the mean rapidity of forward-going protons $\langle y_{\rm c.m.} \rangle$ is 0.87, so the mean longitudinal velocity is $\langle \beta_z^{\rm c.m.} \rangle = \tanh\langle y_{\rm c.m.} \rangle = 0.70$. The mean transverse momentum $\langle p_t \rangle$ is 610 MeV/c, and the mean energy $\langle E_{\rm c.m.} \rangle$ is 1.79 GeV, so the mean transverse velocity $\langle \beta_t^{\rm c.m.} \rangle = \langle p_t \rangle / \langle E_{\rm c.m.} \rangle = 0.34$, about half of the mean longitudinal velocity. The observed shape of the rapidity distribution is indeed well reproduced by a source expanding longitudinally with velocity 0.6–0.7 [16,17]. From consideration of transverse momentum spectra of different particle species, as discussed in Sec. IV A above, a transverse expansion velocity of about 0.24–0.30 can be deduced [13,16], indicating that longitudinal expansion exceeds transverse expansion by a factor of about 2. A study of longitudinal velocities β_z vs time in the hadronic cascade model RQMD [17] has shown a steep decrease during the first few fm/c after the start of the collision, followed by a gradual increase until pions and protons have the same longitudinal velocity of about 0.6. This result supports the hypothesis of strong stopping and subsequent longitudinal expansion that explained inclusive E_t and N_c distributions [21].

Also plotted in Fig. 12 are rapidity distributions from the ARC [22] and RQMD [23] hadronic cascade codes. These results are obtained by imposing experimental cuts on the events generated by the models, not by selecting the impact parameter; the total charged particle multiplicity into the acceptance of the E814 multiplicity detector is selected just as in the data. The overall agreement is good, though at midrapidity both models lie above the data. This discrepancy could be resolved by increasing the values of T_B we use to compute dN/dy below $y = 2.4$, which would in fact be closer to E802's measurement of T_0, but it would worsen our agreement with their measurement of dN/dy (see below).

Both models predict small peaks at target and beam rapidities ($y = 0$ and 3.4) which are not present in the data. The model predictions do not exhibit such behavior in the asymmetric system Si + Pb, however [2]. Since the peaks are only present in the nearly symmetric system, where full overlap occurs with vanishing probability, they are probably due to details in the nuclear surface parametrization.

The proton rapidity distribution measured by E802 [11] in Si + Al for the upper 7% of the geometric cross-section is also plotted in the top panel of Fig. 12. Again, the solid triangles are the directly measured data; the open ones are the same data reflected about midrapidity. These data lie below ours at midrapidity, but they are for much less central collisions. For Si + Pb collisions (shown in Fig. 14 below) we see significant changes in dN/dy with centrality increasing even well beyond the value of $\sigma/\sigma_{\rm geo} \approx 10\%$ expected for full nuclear overlap in a simple geometric model, and we observe a signifi-

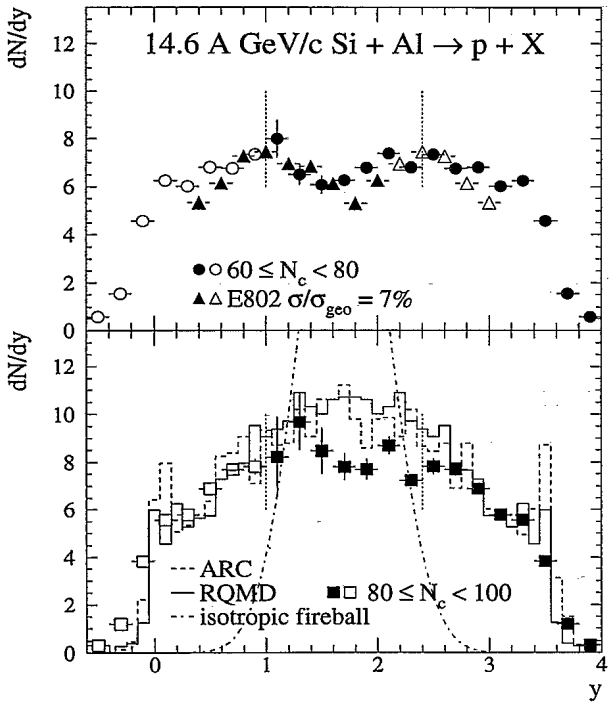

FIG. 12. Proton rapidity distributions for Si + Al. The top panel compares the data for $\sigma/\sigma_{\rm geo} = 2\%$ with data measured by E802 for $\sigma/\sigma_{\rm geo} = 7\%$ [11]. The bottom panel compares the data for $\sigma/\sigma_{\rm geo} = 0.2\%$ with several models.

cant increase at midrapidity with increasing centrality in the Si + Al data in Fig. 11 even in very central collisions. Therefore the larger dN/dy values in our data at $\sigma/\sigma_{\rm geo} = 1.7\%$ and 0.2% as compared to the more peripheral E802 data are expected. Note that in fact for the points at midrapidity we have used slope constants below the ones measured by E802 for more peripheral collisions (see Fig. 8).

With decreasing N_c, one observes the formation of a sharper shoulder, though still not a peak, near beam rapidity in the Si + Al proton rapidity distribution, and a corresponding decrease in the central region. The decrease at midrapidity is somewhat larger than the increase at the forward rapidities, however. Table I shows the integral $N_p \equiv 2\int_{1.72}^{4.0} dN/dy \cdot dy$ of the proton rapidity distribution in each N_c bin for the two different extrapolations of T_B (N_p^A and N_p^B) and the number of statistical standard deviations N_σ by which the two integrals differ for each extrapolation. This demonstrates that the increase in total proton multiplicity with increasing N_c is significant. Note that this does not include the possible effect of an increase in T_B with centrality; where a slope is not measured, dN/dy is computed using the same value of T_B at a given rapidity for each centrality. The increase may be an effect of triggering on extremely large charged particle multiplicities.

Baryon number, charge, and isospin are of course still conserved, but the overall proton multiplicity may be affected by production of hyperons, light nuclei, proton-antiproton pairs (although negligible here [24]), and charge exchange. If more protons are produced due to charge exchange, the conservation laws imply fewer neutrons and more negative than positive and neutral pions. Requiring an increase in charged particle multiplicity essentially selects more resonance decays into charged particles, e.g., $\Delta^0 \to p\pi^-$ vs $\Delta^0 \to n\pi^0$. That this is a plausible explanation for this effect is in fact demonstrated by a similar variation of N_p with N_c in both ARC and RQMD, as shown in Table I. Note that in spite of Λ production, at these large values of N_c, the total number of protons is greater than 29 in the models, significantly exceeding the 27 protons of the target and projectile nuclei. This effect underscores the importance of implementing experimental trigger conditions properly in models when comparing to data.

The total number of protons N_p^B reported in Table I for each centrality is somewhat less than the corresponding numbers from ARC and RQMD. Although this discrepancy is of the same order as the systematic error, we still have to consider protons lost to production of hyperons and light nuclei. To estimate the effect of Λ hyperon production on the proton rapidity distribution, we used the GEANT package. We generated Λ particles with a Gaussian rapidity distribution having unit σ as observed by E810 [25] and a Boltzmann-like transverse momentum distribution having $T_B = 160$ MeV independent of rapidity. These generated particles were tracked through the apparatus by GEANT, allowing them to decay along the way. For charged particles (protons and negative pions) from these decays that struck the tracking chambers and scintillators downstream and also pointed back into the magnet aperture, the momenta and flight path lengths were reconstructed in the same way as the data. GEANT also allowed computation of the time of flight of each particle. Using these reconstructed momenta, path lengths, and times of flight, we calculated the "masses" of the particles via $m = p/\beta\gamma$, identified protons and computed the rapidity and transverse momentum spectra of these decay products as the analysis routine did with the data. The rapidity distribution of these reconstructed protons is shown in Fig. 13.

For each Λ that decays into a proton and negative pion (64%), we detect an average of 0.51 proton. Considering associated production in a system with nearly equal proton and neutron numbers, each Λ produced removes 0.5 proton from the system on average. For each Λ produced, therefore, we lose an average of $0.5 - 0.64 \times 0.51 = 0.17$ proton. Reference [25] indicates that there are 2.5 Λ particles produced per collision, so we estimate an average of

TABLE I. Total proton multiplicity N_p in Si + Al for different charged-particle multiplicity bins. The proton multiplicity $N_p^{\rm tot} \equiv N_p^B + 1.4$ in the third column is adjusted for Λ hyperon and deuteron production (see text). The numbers in parentheses for RQMD and ARC in the last columns include expected Λ hyperon decays not present in the calculations. Errors are statistical.

N_c	N_p^A	N_p^B	$N_p^{\rm tot}$	$N_p^{\rm ARC}$	$N_p^{\rm RQMD}$
70	23.0 ± 0.1	25.3 ± 0.2	26.7 ± 0.2	29.1 (29.9)	29.2 (30.0)
90	23.5 ± 0.3	26.3 ± 0.3	27.7 ± 0.3	29.8 (30.6)	29.7 (30.5)
N_σ	1.6	2.8	2.8		

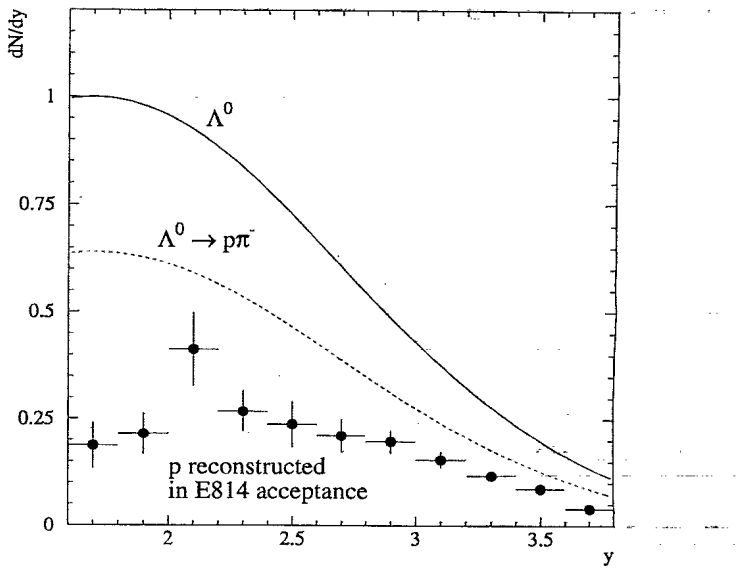

FIG. 13. Rapidity distribution of charged tracks identified as protons from lambda decay in a GEANT simulation. The solid curve is the simulation input, chosen to resemble the measurement of E810 [25] for Si + Si. The dashed curve is the solid one multiplied by the 64% branching ratio for lambda decay into protons and negative pions. The points indicate the multiplicity of those particles accepted in the E814 apparatus and reconstructed as protons.

0.43 proton lost to Λ production and decay per collision.

Next we consider the final-state protons bound in nuclei. In Sec. IV C below, we will show good agreement for the low-transverse-momentum deuteron yields from both E814 and E802, despite differences in acceptance and centrality. We therefore confidently use the overall deuteron yield of 1.0 per collision reported by Parsons [26] for Si + Al. A measurement of $A = 3$ nuclei by E814 [27] indicates that for these purposes nuclei heavier than deuterons can be neglected. We estimate that $0.43 + 1.0 \approx 1.4$ protons are not visible in the experimental data due to production of hyperons and light nuclei. Note that in the RQMD and ARC computations, the Λ particles produced do not decay. If 2.5 Λ particles are produced per collision, in accordance with the E810 data [25], 1.6 will decay to protons and of those 0.82 will be reconstructed in our acceptance, so the proton multiplicity from the model predictions should be increased by 0.8 for purposes of this comparison, as indicated by the numbers in parentheses in the last column. As indicated in Table I, $N_p^{\rm tot} \equiv N_p^B + 1.4$, which includes the protons lost to hyperon and deuteron production, is still less than the models by 2–3 protons, but this difference is within the systematic errors.

Next we turn to proton rapidity distributions in the asymmetric system Si + Pb, wherein the projectile completely overlaps the target nucleus in the upper 10% of the geometric cross-section. In Fig. 14 we plot dN/dy for several different centrality bins in Si + Pb collisions. We observe a very systematic decrease at forward rapidities and a corresponding increase at midrapidity with increasing centrality. As noted above, this effect persists well beyond the value of N_c expected for full overlap between the Si and Pb nuclei. This again emphasizes the importance of applying proper centrality cuts when comparing data to models or other experiments. For the least central events ($\sigma/\sigma_{\rm geo} < 16.2\%$), in which the Si and Pb nuclei do not fully overlap, a shoulder begins to develop at $y = 3.4$, but for the higher centralities, there is no indication of any shoulder or peak at beam rapidity, indicating an absence of nuclear transparency. Our data at $\sigma/\sigma_{\rm geo} = 8.6\%$ agree well with the E802 data for the top 7% of the geometric cross section [11].

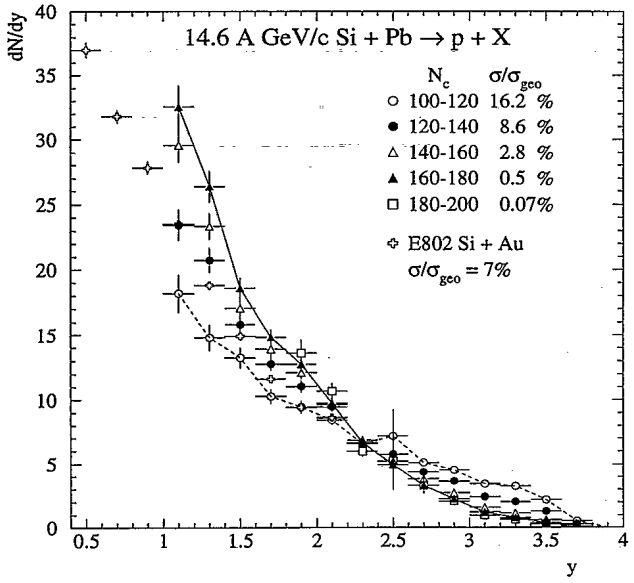

FIG. 14. Rapidity distributions dN/dy for Si + Pb for different centralities from E814 and for Si + Au from E802 [11].

C. Deuteron-proton ratios

We also observe deuterons in this data set. Because their rate is much lower than that of the protons, background from the tail of the proton distribution and from misidentified tracks becomes a serious consideration. To estimate the magnitude of this background, we analyzed the mass spectrum in each 1 GeV/c momentum bin (cf. Fig. 4), fitting the sum of two Gaussian peaks and the sum of an exponential and a constant as background to the region occupied by protons and deuterons. The parameters thus extracted were used to compute the ratio of the number of counts inside the deuteron gate used in the analysis to the number of deuterons in the Gaussian peak, above the background. The gate was determined visually to be the region of the mass axis where the deuteron peak was clearly visible. This background—for each target—was parametrized by a smooth function of momentum and used to correct the yields observed in the data. The background varies between 20 and 60 %. We estimate that this parametrization introduces a systematic uncertainty of about 20 % into the low-transverse-momentum deuteron yields presented here.

Figure 15 shows low-transverse-momentum invariant deuteron yields determined from the present data. These yields are averaged over $p_t < 150$ MeV/c, where the spectra are very flat. Also shown are extrapolations to $p_t = 0$

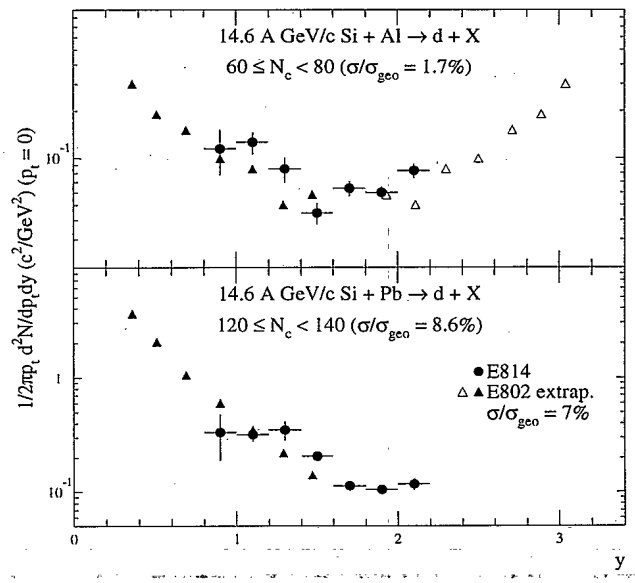

FIG. 15. Low-transverse-momentum invariant deuteron yields. Along with the present data are shown extrapolations to $p_t = 0$ of data from E802 [7] measured at larger p_t for Si + Al, Au collisions.

of the E802 data [7] using their measured fit parameters. The agreement is very good, especially considering the slight differences in centrality, target, and the uncertainty of the extrapolation. Figure 16 shows low-transverse-momentum deuteron-proton ratios dN_d/dN_p for the Al and Pb targets and different centralities. The observed values are low, about 1.5–3 %, and show little dependence on centrality or rapidity. The agreement between the present deuteron yields and results obtained earlier in a different configuration of E814 [27] over a smaller rapidity range is very good. Note that the ratios of the p_t-integrated deuteron and proton yields measured by E802 [7] are larger—about 5 %—because the measured deuteron slope constants are much larger than those of the protons.

Figure 16 also shows for Si + Al the prediction of an isotropic thermal model for the deuteron-proton ratio [cf. Eq. (8)]:

$$\frac{dN_d}{dN_p} = \exp\left(-\frac{(m_d - m_p)\cosh(y - y_{\text{c.m.}}) - (\mu_d - \mu_p)}{T}\right) \tag{12}$$

$$\approx \exp\left(-\frac{m_n \cosh(y - y_{\text{c.m.}}) - \mu_B}{T}\right), \tag{13}$$

where $m_d \approx 1.88$ GeV/c^2 is the deuteron mass, $m_{p,n}$ are the nucleon masses, $\mu_p = \mu_B = 510$ MeV is the baryon chemical potential, obtained from consideration of the volume and temperature [28], $\mu_d = 2\mu_B$ is the deuteron chemical potential, and $T = 140$ MeV is the temperature.

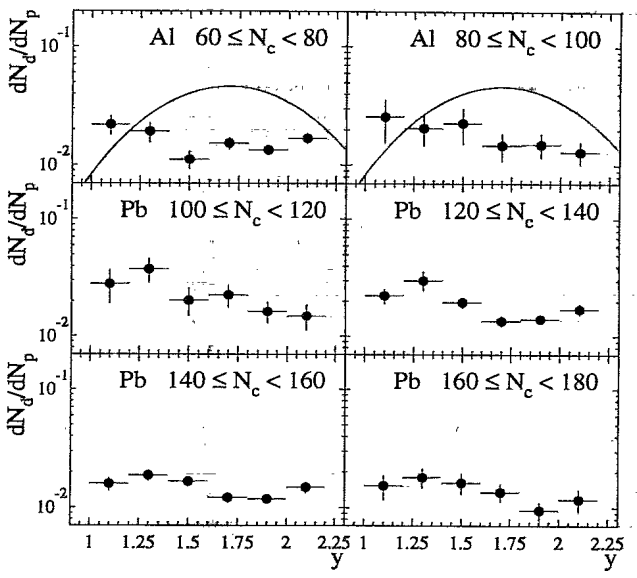

FIG. 16. Low-transverse-momentum deuteron-proton ratios vs rapidity for 14.6A GeV/c Si + Al, Pb → $p, d + X$ at different centralities. The curves plotted in the top two panels for the Al target are the predictions of an isotropically emitting thermal model with 140 MeV temperature and 510 MeV baryon chemical potential.

The temperature and the baryon chemical potential fix the magnitude of this ratio. The isotropic thermal curves (solid lines in Fig. 16) peak very sharply at midrapidity, in clear disagreement with the rather flat distribution of the data. Although a thermal model explains the data qualitatively [27], e.g., it predicts the overall deuteron-proton ratio—it does not describe the differential distributions. This discrepancy appears to be another indication for longitudinal expansion. The protons have already been seen to be much wider than an isotropic distribution, and the deuterons are even wider.

V. CONCLUSIONS

We have seen that proton transverse mass spectra are well described by Boltzmann parametrizations, a necessary though not sufficient condition for a thermalized system. Values of T_B as high as 150 MeV are observed for $y > 2.5$. These large values, especially when considered simultaneously with those for other particle species, give a strong indication for transverse flow. For Si + Pb these values increase systematically with increasing centrality, even beyond the point of full overlap between the two nuclei. This result could indicate the onset of a phase transition.

We observe no significant nuclear transparency either in Si + Pb or in the symmetric system Si + Al. No peak is visible at or near beam rapidity in either system for very central collisions. This indicates a large degree of stopping and that a large baryon density is achieved in these collisions. In fact, to the extent that models like ARC and RQMD describe well the distributions of baryons in phase space, we can take seriously their predictions for configuration space distributions. RQMD [29] predicts a peak baryon density 7 times the normal nuclear value for central Si + Au collisions and an energy density of 1.75 GeV/fm^3, while ARC [30] predicts a peak baryon density around 8 times that of normal nuclear matter.

The rapidity distribution for Si + Al, however, is much wider than that for an isotropically emitting thermal system, which may indicate only partial stopping, but more likely points to longitudinal expansion of the system after the collision. Deuteron-proton ratios at $p_t = 0$ are much flatter than for an isotropic thermal system as well, also suggesting longitudinal flow. Studies using RQMD support this hypothesis, indicating full stopping followed by longitudinal expansion.

The integral of the Si + Al rapidity distribution, which is the total number of protons in the final state, varies with charged particle multiplicity N_c. This effect is present in both ARC and RQMD as well. Selection of the charged particle multiplicity biases resonance decays to influence the number of protons in the final state.

The rapidity distributions of protons in both Si + Al and Si + Pb change significantly in even the most central collisions, well beyond full geometric overlap in the case of Si + Pb, demonstrating the importance of careful centrality selection when comparing data to models or other experiments.

ACKNOWLEDGMENTS

The E814 Collaboration wishes to thank the Brookhaven Tandem and AGS staffs, especially H. Brown and W. McGahern, for invaluable assistance. We also thank R. Hutter and J. Sondericker for their excellent technical support which has been essential to the success of this experiment. We are very grateful for financial support received from the U.S. DoE and NSF as well as the Canadian NSERC and the CNPq of Brazil.

[1] See, e.g., R. Anishetty, P. Koehler, and L. McLerran, Phys. Rev. D **22,** 2793 (1980); or J. D. Bjorken, in *Current Induced Reactions,* Proceedings of the International Summer Institute on Theoretical Particle Physics, Hamburg 1975, edited by J. G. Körner, G. Kramer, and D. Schildknecht (Springer-Verlag, Berlin, 1976), p. 93.

[2] E814 Collaboration, J. Barrette *et al.*, Z. Phys. C **59,** 211 (1993).

[3] E814 Collaboration, J. Barrette *et al.,* Phys. Rev. C **46,** 312 (1992).

[4] D. G. Cassel and H. Kowalski, Nucl. Instrum. Methods **185,** 235 (1981).

[5] E814 Collaboration, J. Barrette *et al.,* Phys. Rev. C **45,** 819 (1992).

[6] G. Birkhoff and S. MacLane, *A Survey of Modern Algebra,* revised ed. (MacMillan, New York, 1953), p. 114.

[7] C. G. Parsons, Ph.D. dissertation, MIT, 1992.

[8] R. Brun *et al.,* GEANT 3 Users Guide, CERN Data Handling Division Report No. DD/EE/84-1, 1984 (unpublished).

[9] B. Cole, in *HIPAGS '93,* Proceedings of Heavy Ion Physics at the AGS, Cambridge, Mass., 1993, edited by G. S. F. Stephans, S. G. Steadman, and W. L. Kehoe (MITLNS-2158), p. 313.

[10] E814 Collaboration, J. Barrette *et al.,* Phys. Rev. Lett. **64,** 1219 (1990).

[11] E802 Collaboration, T. Abbott *et al.,* Phys. Rev. C **50,** 1024 (1994).

[12] J. Stachel and G. R. Young, Annu. Rev. Nucl. Part. Sci. **42,** 537 (1992).

[13] E814 Collaboration, J. Stachel, in *Quark Matter '93,* Proceedings of the Tenth International Conference on Ultra-relativistic Nucleus-Nucleus Collisions, Borlänge, Sweden, 1993, edited by E. Stenlund *et al.* [Nucl. Phys. **A566,** 183c (1994)].

[14] G. E. Brown, J. Stachel, and G. M. Welke, Phys. Lett. B **253,** 19 (1991).

[15] E814 Collaboration, T. K. Hemmick, in *Quark Matter '93* [Nucl. Phys. **A566,** 435c (1994)].

[16] E814 Collaboration, N. Xu, in *Proceedings of the Tenth Winter Workshop on Nuclear Dynamics, Snowbird, Utah, 1994,* edited by W. Bauer (in press).

[17] P. Braun-Munzinger, J. Stachel, J. P. Wessels, and N. Xu, Report No. SUNY-RHI-94-11 [Phys. Lett. B (submitted)].

[18] J. B. Costales, Ph.D. dissertation, MIT, 1990.

[19] L. van Hove, Phys. Lett. **118B,** 138 (1982).

[20] P. V. Ruuskanen, Z. Phys. C **38,** 219 (1988); M. Kataja, P. V. Ruuskanen, L. McLerran, and H. von Gersdorff, Phys. Rev. D **34,** 2755 (1986).

[21] P. Braun-Munzinger and J. Stachel, Phys. Lett. B **216,** 1 (1989).

[22] T. J. Schlagel, S. H. Kahana, and Y. Pang, Phys. Rev. Lett. **69,** 3290 (1992).

[23] H. Sorge, H. Stöcker, and W. Greiner, Ann. Phys. (N.Y.) **192,** 266 (1989); A. Jahns, H. Sorge, H. Stöcker, and W. Greiner, Z. Phys. A **341,** 243 (1992); and private communication.

[24] E814 Collaboration, J. Barrette *et al.*, Phys. Rev. Lett. **70,** 1763 (1993).

[25] E810 Collaboration, S. E. Eiseman *et al.*, Phys. Lett. B **297,** 44 (1992).

[26] C. G. Parsons, in *HIPAGS '93* [9], p. 72.

[27] E814 Collaboration, J. Barrette *et al.*, Phys. Rev. C **50,** 1077 (1994).

[28] E814 Collaboration, P. Braun-Munzinger in *Hot and Dense Matter,* Proceedings of the NATO ASI, Bodrum, Turkey, 1993 (Plenum, N.Y., in press).

[29] H. Sorge, A. von Keitz, R. Mattiello, H. Stöcker, and W. Greiner, Phys. Lett. B **243,** 7 (1990).

[30] Y. Pang, T. J. Schlagel, and S. H. Kahana, Phys. Rev. Lett. **68,** 2743 (1992); and private communication.